Correction 08/07/2013

Looking for jarosite on Mars: the low-temperature crystal structure of jarosite

Stuart J. Mills[1*], Fabrizio Nestola[2], Volker Kahlenberg[3], Andrew G. Christy[4], Clivia Hejny[3], Günther J. Redhammer[5]

[1]Geosciences, Museum Victoria, GPO Box 666, Melbourne 3001, Victoria, Australia

[2]Dipartimento di Geoscienze, Università di Padova, Via Gradenigo 6, Padova I-35131, Italy

[3]Institut für Mineralogie und Petrographie der Universität Innsbruck, Innrain 52, 6020 Innsbruck, Austria

[4]Centre for Advanced Microscopy, Australian Natioanl University, Canberra, ACT 0200, Australia

[5]Department of Materials Engineering and Physics, University of Salzburg, Hellbrunnerstr. 34, A-5020 Salzburg, Austria

*E-mail: smills@museum.vic.gov.au

Abstract

Single-crystal diffraction of jarosite, $KFe^{3+}_3(SO_4)_2(OH)_6$, has been undertaken at low temperatures that proxy for Martian surface conditions. Room temperature data is consistent with literature data (a = 7.2913(5), c = 17.1744(17) and V = 790.72(11) in R-3m), while the first low temperature data for the mineral is presented (at 253, 213, 173 and 133K). Data collections between 297 and 133 K show strongly anisotropic thermal expansion, with the **c** axis much more expandable than the **a** axis. Much of the anisotropy is due to strong distortion of the KO_{12} polyhedron, which increases by 8 % between 297 and 133 K. The datasets can aid in the identification of jarosite by X-ray diffraction of Martian soils using the Curiosity Rover's CheMin instrument.

Keywords: crystal structure, low temperature, jarosite, Mars, anisotropy, alunite supergroup.

Introduction

Jarosite, $KFe^{3+}_3(SO_4)_2(OH)_6$ (Mills et al. 2009a; Bayliss et al. 2010), has always been a mineral of great interest to mineral scientists, because of its relevance to many areas such as acid mine drainage (e.g., Nordstrom et al. 2000; Welch et al. 2007, 2008, 2009), the mobility of toxic elements (e.g., Kolitsch & Pring 2001) and metallurgical processing (e.g., Dutrizac & Jambor 2000). But it is its discovery on Mars (Klingelhöfer et al. 2004; Farrand et al. 2009) in particular, which has caused a renaissance in research about the formation and stability of the mineral (e.g., Navrotsky et al. 2005; Papike et al. 2006; Golden et al. 2008) and its structural analogues (e.g., Grey et al. 2008, 2009, 2011, 2013; Mills et al. 2010; Scarlett et al. 2010, 2013). Despite this, very few single crystal refinements of jarosite have been made, and none at low temperature. The lack of low-temperature data for jarosite is important, in this case, because the CheMin (Chemistry & Mineralogy X-Ray Diffraction) instrument on the

Curiosity Rover is designed to identify minerals by X-ray diffraction and chemical analysis (Grotzinger et al. 2012), and the surface temperature on Mars is low enough to cause significant change in cell parameters from room-temperature values, or even to drive minerals through phase transitions. The global mean surface temperature is ~202 K (Haberle 2013), while local temperatures may lie within the range of at least 143–273 K (Herri & Chassefière 2012). We note that the wide range of low temperatures on Mars may also have significant effects on other measurements (e.g. spectroscopic) used for detection and identification of minerals such as jarosite.

Jarosite is a member of the large alunite supergroup of minerals (Mills et al. 2009a; Bayliss et al. 2010), and participates in a wide range of solid solutions where the K^+ may be replaced by other species such as Na^+ or H_3O^+, Fe^{3+} by Al^{3+}, and S^{6+} by P^{5+} or As^{5+}. Furthermore, members of the supergroup may deviate from the ideal $AB_3(TO_4)_2X_6$ stoichiometry. There may be vacancies on the large interlayer *A* sites (as in plumbojarosite, $(Pb_{0.5}\square_{0.5})Fe_3(SO_4)_2(OH)_6$ — Szymański, 1985; Mills et al. 2009b), interstitial small cations (kolitschite, $PbZn_{0.5}Fe_3(AsO_4)_2(OH)_6$ — Mills et al. 2008; Grey et al. 2008) or, in material synthesised at low temperatures, vacancies on the octahedral *B* sites (Scarlett et al. 2010; Grey et al. 2011). In the latter two cases, ordering of the defects reduces the symmetry from rhombohedral to *C*-centred monoclinic. The unit cell parameters vary significantly with all of these substitutions, although the *a*-axis is more sensitive to the content of the *B* site and the *c*-axis to the content of the interlayer *A* site (cf. Drouet et al. 2004).

It is likely that some "jarosite" minerals present on Mars depart considerably from the end-member jarosite studied here. Morris et al. (2006) indicate that for samples examined at Meridiani Planum, at least, $Na^+ > K^+ > H_3O^+$ with possible Al^{3+} substitution for Fe^{3+}. This

implies that mineral is not jarosite *sensu stricto* but natrojarosite, with solid solution towards jarosite, hydroniumjarosite and natroalunite. Milliken et al. (2013) report infrared spectra from the region of Ius and Melas Chasmata that they interpret as from H_3O-bearing, Fe-deficient jarosite. The simulated Martian acid-sulfate alteration experiments of McCollom *et al*. (2013a,b) suggest that the alunite-supergroup phase formed by alteration of mafic pyroclastics should be Fe-rich natroalunite, rather than jarosite. Hence, a range of alunite-supergroup solid solutions may be present on Mars. Physical properties, including temperature-dependent diffraction behaviour, can most easily be estimated for such compositionally intermediate phases by interpolation from good-quality data for the end-members. This paper constitutes a first step in the assembly of a dataset suitable for such interpolation, where we have investigated the single crystal structure of a sample of natural jarosite between 297 and 133 K, covering the range of surface temperatures experienced by Mars.

Experimental

Sample

Although an analysis corresponding to jarosite was first reported from lignite seams at Kolosuruk (Korozluky, Czech Republic) by Rammelsberg (1838), he referred to the mineral only as "gelbeisenerz" (yellow iron ore). The first use of the name 'Jarosit' for the mineral was by Breithaupt (1852) for material from the Jaroso Ravine, Sierra Almagrera, Andalusia, Almeria, Spain, which is therefore regarded as the type locality. The sample of endmember $KFe^{3+}_3(SO_4)_2(OH)_6$ jarosite used in the study (M20912) was from the type locality and was obtained by Museum Victoria from Dr August Krantz in the 1850s. Thus, this specimen would have not been collected long after the type description was published. The specimen consists of clusters of honey-brown crystals up to about 1 mm across, coating cavities in

101 massive hematite rock. Several crystals were selected then used for the single crystal study.
102 The jarosite–hematite association is prevalent on Mars, the most notable example being that
103 at Meridiani Planum (Klingelhöfer et al. 2004; Golden et al. 2008).
104
105 *X-ray diffraction*
106 A prismatic brownish-transparent single-crystal (dimensions: 0.04 x 0.05 x 0.09 mm) of good
107 optical quality when observed under a petrographic microscope was selected for the X-
108 diffraction experiments and mounted on the tip of a glass fibre using nail polish. X-ray
109 diffraction data were acquired at five temperatures (297, 253, 213, 173 and 133 K) with an
110 Oxford Diffraction Gemini-R Ultra diffractometer equipped with a Ruby CCD detector and
111 graphite-monochromated MoK_α radiation. For the low-temperature studies, the crystal was
112 cooled using an Oxford Cryosystems 700 Plus open-flow nitrogen gas device. The absolute
113 temperature uncertainty of this device, determined from a series of calibration experiments, is
114 about 1.5 K. Temperature stability during the data collection was ± 0.2 K. Integration and
115 data reduction, including Lorentz-polarization as well as a semi-empirical absorption
116 correction, were performed with the CrysAlis software package. Over the whole temperature
117 range, the crystal diffraction spots could be indexed on the *R*-centred trigonal unit cell typical
118 for jarosite. No indications of a structural phase transformation were observed. A detailed
119 summary of the data collection strategy can be found in **Table 1**. Fractional coordinates and
120 atom displacement parameters are provided in **Table 2**, and selected interatomic distances in
121 **Table 3**.
122
123 **Results**
124 Jarosite has a rhombohedral alunite-type structure (e.g. Blount, 1974), consisting of layers
125 parallel to (0001) of corner-sharing $FeO_2(OH)_4$ octahedra and SO_4 tetrahedra, stacked along

126 **c**. K atoms at the origin of the cell are in 12-fold coordination. The $Fe(O,OH)_6$ octahedra each
127 share corners with four neighbours via the OH^- anions to form a planar kagomé network with
128 3- and 6-fold rings, which can also be described as hexagonal tungsten bronze (HTB)-type
129 layers (**Fig. 1**). The O^{2-} anions of the $Fe(O,OH)_6$ octahedra in each 3-ring link to a sulfur
130 either above or below the plane of the Fe layer. Successive layers are interconnected via
131 hydrogen bonds from H to sulfate O1 of an adjacent layer, as well as through weak K□O
132 bonds. The room temperature dataset (297 K) is consistent with those reported for
133 refinements of jarosite with a similar composition: <K□O> is 2.896, <Fe□O> is 2.006 and
134 <S□O> is 1.477 Å, compared to 2.876, 2.004 and 1.498 Å, respectively for
135 $K_{0.953}H_3O_{0.047}Fe^{3+}{}_3(SO_4)_2(OH)_6$ (Basciano & Peterson 2007). Note that the long S□O bond
136 length in $K_{0.953}H_3O_{0.047}Fe^{3+}{}_3(SO_4)_2(OH)_6$ may be an artefact due to refining powder data
137 using the Rietveld method.
138
139 The low-temperature investigation performed in this study reveals a very strong anisotropy in
140 the thermal expansion of jarosite, with the *c*-axis being much more expandable than the *a*-
141 axis. **Table 4** shows the variation of the two cell parameters as a function of temperature. The
142 *a*-axis length remains practically unchanged over the temperature range investigated (0.0024
143 Å = 0.03% relative variation between maximum and minimum values), although what
144 variation there is appears to be non-montonic, with positive expansivity at low temperature
145 up to a maximum *a* parameter near 253 K, and then negative expansivity to 297 K (**Table 4**).
146 The changes are small, but the possible change in sign of expansivity merits further study.
147 The *c*-axis however, decreases in length with decreasing temperature by about 0.072 Å,
148 monotonically but with distinct curvature. **Figure 2a** shows the evolution with temperature of
149 the two axes. The *y* scale is the same for the two axes, in order to emphasise the difference in
150 absolute expansivity along the two axes. In **Figure 2b,** the unit cell volume is plotted against

151 temperature, showing a decrease by about 4.0 Å^3 (~0.5 %) from 297 to 133 K that is almost
152 linear with temperature, due to the curvatures of *a*-*T* and *c*-*T* trends compensating for each
153 other.
154
155 A linear approximation to the volume thermal expansion can be calculated as $\alpha_V = [(V - V_0) /$
156 $V_0]/\Delta T$ (e.g. Cameron et al. 1973). For our sample and a ΔT calculated between 297 and 133
157 K we obtain $\alpha_V = 3.10(5)\times10^{-5}\ K^{-1}$.
158
159 The cell parameters of this study extrapolate to significantly smaller values at very low
160 temperatures than those obtained by Inami et al. (2000) using powder neutron diffraction at
161 10 K (*a* = 7.2999(3) Å and *c* = 7.3013(8) Å) and on deuterated material at 7 K (*a* = 7.3013(8)
162 Å and *c* = 17.097(1) Å). However, they note that there is a transition into a long-range
163 ordered antiferromagnetic state at 65 K, and associated structural relaxation may account for
164 the discrepancy. Conversely, our 297 K data are in good agreement with the 298 K data from
165 the powder neutron diffraction study of Xu et al. (2010), and our plots of **c** and *V* against
166 temperature (Figure 2a,b) extrapolate into theirs for the range *T* = 298–575 K with only slight
167 breaks in slope. Our *a*-axis at 297 K is also close to that of Xu et al. (2010), however, our
168 data do not lie on their trend for $T \geq 350$ K of **a** increasing nonlinearly with *T*. The *a*-axis of
169 Xu *et al*. (2010) increases by only 0.09 % over 350–575 K, while **c** increases an order of
170 magnitude more (0.91 %), so the extreme anisotropy in expansion is maintained to high
171 temperatures. In combination, the datasets of Inami et al. (2000), Xu et al. (2010) and this
172 study, suggest that the jarosite *a*-axis reaches a minimum value near 300 K, varies by only a
173 small amount, but possibly in a complex fashion, over the temperature range of our study,
174 and increases again below the magnetic transition at 65 K.
175

In order to explain the strong axial anisotropy, and, generally, the behaviour as a function of temperature, a careful analysis of the evolution of the jarosite crystal structure is necessary. Examination of the bond lengths indicates that <K□O> shows the largest variation (a decrease by about 0.4%, **Table 3**), while <Fe□O> remains practically constant and <S□O> shows an increase with decreasing T (by about 0.3 %). The analysis of the site polyhedron volumes (calculated using the software IVTON by Balić-Žunić and Vickovic 1996) confirm the trends shown by the bond lengths. Over the range 297□133 K, the KO_{12} polyhedron decreases in volume by about 1 %, the FeO_6 polyhedron does not show significant variation, and the SO_4 tetrahedron increases its volume by about 0.8 %. **Figure 3** shows the evolution of KO_{12}, FeO_6 and SO_4 volumes with T.

We also consider the temperature evolution of distortion for these polyhedra. The volume distortion parameter used here quantifies the volume deficit of the polyhedron as compared to an ideal equivalent. First, a sphere of best fit is found for the real polyhedron and the ratio of sphere volume to polyhedron volume V_s/V_r calculated (Balić-Žunić and Makovicky 1996; Balić-Žunić 2007). Ideal polyhedra are chosen for reference, which in this case are the regular tetrahedron, regular octahedron and regular cuboctahedron for S, Fe and K respectively. The volume ratios V_s/V_i are calculated for these shapes inscribed in a sphere, and the distortion $\upsilon = 1 - (V_s/V_i)/(V_s/V_r)$ (Makovicky and Balić-Žunić 1998; Nestola et al. 2008). The advantage of this parameter is that it measures only distortions due to the arrangement of atoms forming the vertices of the polyhedron alone, and decouples these from distortion due to the relative position of the central atom and surrounding atoms. As a result, the volume distortion can even be calculated for structural voids when necessary.

An analysis of the polyhedron volume of the KO_{12} polyhedron shows that it is extremely distorted (distortion at 297 K = 0.0168, **Table 3**) and that its distortion decreases with decreasing the temperature by about 8 % (**Figure 4a**). The distortion of the KO_{12} polyhedron is strongly related to the polyhedron volume behaviour (**Figure 4b**). Plotting the KO_{12} volume against the *c*-axis (the most compressible one) shows a strong relation (**Figure 4c**) and that the contraction along the *c*-axis is governed not only by the volume decrease of the KO_{12} polyhedron but also by its volume distortion.

The FeO_6 octahedron is much more regular than KO_{12}, distortion of the FeO_6 being an order of magnitude lower: 0.0014 at 297 K (**Table 3**). More importantly, it does not show any variation over the temperature range investigated (**Table 3**). The SO_4 tetrahedron shows negligible volume distortion at all temperatures.

Implications

Given the significant change in the jarosite unit cell over the temperature range of this study, this dataset can aid in the identification of the mineral via X-ray diffraction of Martian soils using the Curiosity Rover's CheMin instrument. It is important to note, however, that extensive solid solutions occur between members of the alunite supergroup, so further studies on natrojarosite, natroalunite, alunite and hydroniumjarosite at low temperature will be required to generate a broad crystallographic dataset which will cover the range of compositions likely to be present, and to allow correct mineral assignment of Martian "jarosites". Furthermore, elemental analysis will be desirable to confirm such identifications, and spectroscopic methods are required to identify the H_3O^+ ion, which readily substitutes for K^+.

Acknowledgements

We thank Tom McCollom and an anonymous reviewer who provided helpful comments on the manuscript.

References

Balić-Žunić, T. (2007) Use of three-dimensional parameters in the analysis of crystal structures under compression. In A. Grzechnik, Ed., Pressure Induced Phase Transitions. Transworld Research Network, Kerala, India.

Balić-Žunić, T. and Vickovic, I. (1996) IVTON program for the calculation of geometrical aspects of crystal structures and some chemical applications. Journal of Applied Crystallography, 29, 305306.

Balić-Žunić, T. and Makovicky, E. (1996) Determination of the Centroid or "the Best Centre" of a Coordination Polyhedron. Acta Crystallographica, B52, 78–81.

Basciano, L.C. and Peterson, R.C. (2007) Jarosite–hydronium jarosite solid-solution series with full iron site occupancy: Mineralogy and crystal chemistry. American Mineralogist, 92, 1464□1473.

Bayliss, P., Kolitsch, U., Nickel, E.H. and Pring, A. (2010) Alunite supergroup: recommended nomenclature. Mineralogical Magazine, 74, 919□927.

Blount, A.M. (1974) The crystal structure of crandallite. American Mineralogist, 59, 41□47.

Breithaupt, J.F.A. (1852) Beschreibung der zum Theil neuen Gang-Mineralien des Baranco Jaroso in der Sierra Almagrera. Berg- und hüttenmännisches Zeitung, mit besonderer Berucksichtigung der Mineralogie und Geologie, Freiberg, 11, 65□69.

Cameron, M., Sueno, S., Prewitt, C.T. and Papike, J.J. (1973) High-temperature crystal chemistry of acmite, diopside, hedenbergite, jadeite, spoumene, and ureyite. American Mineralogist, 58, 594□618.

Drouet, C., Pass, K.L., Baron, D., Draucker, S. and Navrotsky, A. (2004) Thermochemistry of jarosite-alunite and natrojarosite-natroalunite solid solutions. Geochimica et Cosmochimica Acta, 68, 2197□2205.

Dutrizac, J.E. and Jambor, J.L. (2000) Jarosites and Their Applications in Hydrometallurgy. Pp. 405□452 in: Sulfate Minerals: Crystallography, Geochemistry, and Environmental Significance (C.N. Alpers, J.L. Jambor and D.K Nordstrom, editors). Reviews in Mineralogy and Geochemistry, 40. Mineralogical Society of America, Washington DC and the Geochemical Society, St Louis, Missouri, USA.

Farrand, W.H., Glotch, T.D., Rice Jr, J.W., Hurowitz, J.A. and Swayze, G.A. (2009) Discovery of jarosite within the Mawrth Vallis region of Mars: Implications for the geologic history of the region. Icarus, 204, 478–488.

Golden, D.C., Ming, D.W., Morris, R.V. and Graff, T.G. (2008) Hydrothermal synthesis of hematite spherules and jarosite: Implications for diagenesis and hematite spherule formation in sulfate outcrops at Meridiani Planum, Mars. American Mineralogist, 93, 1201–1214.

Grotzinger, J.P., Crisp, J., Vasavada, A.R., Anderson, R.C., Baker, C.J., Barry, R., Blake, D.F., Conrad, P., Edgett, K.S., Ferdowski, B., Gellert, R., Gilbert, J.B., Golombek, M., Gómez-Elvira, J., Hassler, D.M., Jandura, L., Litvak, M., Mahaffy, P., Maki, J., Meyer, M., Malin, M.C., Mitrofanov, I., Simmonds, J.J., Vaniman, D., Welch, R.V. and Wiens, R.C. (2012) Mars Science Laboratory mission and science investigation. Space Science Reviews, 170, 5–56.

Grey, I.E., Mumme, W.G., Bordet, P. and Mills, S.J. (2008) A new crystal-chemical variation of the alunite-type structure in monoclinic $PbZn_{0.5}Fe_3(AsO_4)_2(OH)_6$. Canadian Mineralogist, 46, 1355–1364.

Grey, I.E., Mumme, W.G., Mills, S.J., Birch, W.D. and Wilson, N.C. (2009) The crystal chemical role of Zn in alunite-type minerals: Structure refinements for kintoreite and zincian kintoreite. American Mineralogist, 94, 676–683.

Grey, I.E., Scarlett, N.V.Y. and Brand, H.E.A. (2013) Crystal chemistry and formation mechanism of non-stoichiometric monoclinic K-jarosites. Mineralogical Magazine, 77, 249–268.

Grey, I.E., Scarlett, N.V.Y., Bordet, P. and Brand, H.E.A. (2011) Jarosite–butlerite intergrowths in non-stoichiometric jarosites: crystal chemistry of monoclinic natrojarosite–hydroniumjarosite phases. Mineralogical Magazine, 75, 2775–2791.

Haberle, R.M. (2013) Estimating the power of Mars' greenhouse effect. Icarus, 223, 619–620.

Herri, J.-M., and Chassefière, E. (2012) Carbon dioxide, argon, nitrogen and methane clathrate hydrates: Thermodynamic modelling, investigation of their stability in Martian atmospheric conditions and variability of methane trapping. Planetary and Space Science, 73, 376–386.

Inami, T., Nishiyama, M., Maegawa, S. and Oka, Y. (2000) magnetic structure of the kagomé lattice antiferromagnet potassium jarosite $KFe_3(OH)_6(SO_4)_2$. Physical Review B, 61, 12181–12186.

Klingelhöfer, G., Morris, R.V., Bernhardt, B., Shroder, C., Rodinov, D.S., de Souza, P.A., Yen, A., Gellert, R., Evlanov, E.N., Zubkov, B., Foh, J., Bonnes, U., Kankeleit, E., Gutlich, P., Ming, D.W., Renz, F., Wdowiak, T., Squyres, S.W. and Arvidson, R.E. (2004) Jarosite and hematite at Meridiani Planum from Opportunity's Mössbauer spectrometer. Science, 306, 1740–1745.

Kolitsch, U. and Pring, A. (2001) Crystal chemistry of the crandallite, beudantite and alunite groups: a review and evaluation of the suitability as storage materials for toxic metals. Journal of Mineralogical and Petrological Sciences, 96, 67□78.

Makovicky, E. and Balić-Žunić, T. (1998) New measure of distortion for coordination polyhedra. Acta Crystallographica, B54, 766□773.

McCollom, T.M., Robbins, M., Moskowitz, B., Berquó, T.S., Jöns, N., and Hynek, B.M. (2013a) Experimental study of acid-sulfate alteration of basalt and implications for sulfate deposits on Mars. Journal of Geophysical Research: Planets, 118, 577□614.

McCollom, T.M., Ehlmann, B.L., Wang, A., Hynek, B.M., Moskowitz, B. and Berquó, T.S. (2013b) Detection of iron substitution in natroalunite and potential implications for Mars. American Mineralogist, 98,[in this issue]

Milliken, R.E., Swayze, G.A., Arvidson, R.E., Bishop, J.L., Clark, R.N., Ehlmann, B.L., Green, R.O., Grotzinger, J.P., Morris, R.V., Murchie, S.L., Mustard, J.F. and Weitz, C. (2013) Opaline silica in young deposits on Mars. Geology, 36, 847□850.

Mills, S.J., Grey, I.E., Mumme, W.G., Miyawaki, R., Matsubara, S., Bordet, P., Birch, W.D. and Raudsepp, M. (2008) Kolitschite, $Pb[Zn_{0.5},\square_{0.5}]Fe_3(AsO_4)_2(OH)_6$, a new mineral from the Kintore opencut, Broken Hill. Australian Journal of Mineralogy, 14, 63□67.

Mills, S.J., Hatert, F., Nickel, E.H. and Ferraris, G. (2009a) The standardisation of mineral group hierarchies: application to recent nomenclature proposals. European Journal of Mineralogy, 21, 1073□1080.

Mills, S.J., Madsen, I.C., Grey, I.E. and Birch, W.D. (2009b) In situ XRD study of the thermal decomposition of natural arsenian plumbojarosite. Canadian Mineralogist, 47, 683□696.

Mills, S.J., Kampf, A.R., Raudsepp, M. and Birch, W.D. (2010) The crystal structure of waylandite from Wheal Remfry, Cornwall, United Kingdom. Mineralogy and Petrology, 100, 249□253.

Morris, R.V., Klingelhöfer, G., Schröder, C., Rodionov, D.S., Yen., A., Ming, D.W., de Souza Jr., P.A., Wdowiak, T., Fleischer, I., Gellert, R., Bernhardt, B., Bonnes, U., Cohen, B.A., Evlanov, E.N., Foh, J., Gütlich, P., Kankeleit, E., McCoy, T., Mittlefehldt, D.W., Renz, F., Schmidt, M.E., Zubkov, B., Squyres, S.W. and Arvidson, R.E. (2006) Mössbauer mineralogy of rock, soil, and dust at Meridiani Planum, Mars: Opprtunity's journey across sulfate-rich outcrop, basaltic sand and dust, and hematite lag deposits. Journal of Geophysical Research, 111, E12S15, doi: 10.1029/2006JE002791.

Navrotsky, A., Forray, F.L. and Drouet, C. (2005) Jarosite stability on Mars. Icarus, 176, 250□253.

Nestola, F., Boffa Ballaran, T., Balić-Žunić, T. Secco, L. and Dal Negro, A. (2008) The high-pressure behavior of an Al- and Fe-rich natural orthopyroxene. American Mineralogist, 93, 644-652.

Nordstrom, D.K., Alpers, C.N., Ptacek, C.J. and Blowes D.W. (2000) Negative pH and extremely acidic mine waters from Iron Mountain, California. Environmental Science & Technology, 34, 254□258.

Papike, J.J., Karner, J.M. and Shearer, C.K. (2006) Comparative planetary mineralogy: Implications of martian and terrestrial jarosite. A crystal chemical perspective. Geochimica et Cosmochimica Acta, 70, 1309□1321.

Rammelsberg, C. (1838) Mineralogisch-chemische Notizen über Stilpnomelan, schwefelsaure Thonerde und schwefelsaures Eisenoxyd. Annalen der Physik und Chemie, Leipzig, 43, 127□135.

Scarlett, N.V.Y, Grey, I. E. and Brand, H.E.A. (2010) Ordering of iron vacancies in monoclinic jarosites. American Mineralogist, 95, 1590□1593.

Scarlett, N.V.Y., Grey, I.E. and Brand, H.E.A. (2013) In situ synchrotron diffraction studies on the formation kinetics of jarosites. Journal of Synchrotron Radiation, 20, 366□375.

Szymański, J.T. (1985) The crystal structure of plumbojarosite $Pb[Fe_3(SO_4)_2(OH)_6]_2$. Canadian Mineralogist, 23, 659□668.

Welch, S.A., Christy, A.G., Kirste, D., Beavis, S.G. and Beavis, F. (2007) Jarosite dissolution I – trace cation flux in acid sulfate soils. Chemical Geology, 245, 183□197.

Welch, S.A., Kirste, D., Christy, A.G., Beavis, F.R. and Beavis, S.G. (2008) Jarosite dissolution II – reaction kinetics, stoichiometry and acid flux. Chemical Geology, 254, 73□86.

Welch, S.A., Christy, A.G., Isaacson, L. and Kirste, D. (2009) Mineralogical control of rare earth elements in acid sulfate soils. Geochimica et Cosmochimica Acta, 73, 44□64.

Xu, H., Zhao, Y., Vogel, S.C., Hickmott, D.D., Daemen, L.L. and Hartl, M.A. (2010) Thermal expansion and decomposition of jarosite: a high-temperature neutron diffraction study. Physics and Chemistry of Minerals, 37, 73□82.

Figure Captions

Figure 1. (a) Structural layer of jarosite viewed down **c** axis, showing $FeO_2(OH)_4$ octahedra corner-linked to form kagomé net, and triangles of octahedra linked to SO_4 tetrahedra above or below the plane of the layer. Hydrogen atoms indicated by small spheres; outlines of unit cells are dashed. (b) Unit cell of jarosite viewed approximately down [110], showing portions of three layers of the type shown in (a). SO_4 tetrahedra point up into the hexagonal holes in the layer above, or down into the hexagonal holes of the layer below. O-H vectors are directed at apical sulfate oxygens of adjacent layers. Large spheres are 12-coordinated interlayer K^+ ions.

Figure 2. (a) Temperature evolution of *a* and *c* parameters of jarosite. Estimated errors are smaller than symbols used. (b) Variation of unit cell volume with temperature for jarosite.

Figure 3. Variation with temperature of (a) KO_{12} polyhedral volume, (b) FeO_6 polyhedral volume, (c) SO_4 polyhedral volume.

Figure 4. (a) Variation of KO_{12} polyhedral distortion parameter with temperature. (b) Linear correlation between KO_{12} polyhedral volume and distortion parameter. (c) Linear correlation between KO_{12} polyhedral volume and unit cell *c* parameter.

426 Table 1: Data collection and structure refinement details for jarosite.
427

	297 K	253 K	213 K	173 K	133 K
Structural Formula			$KFe_{2.77}Al_{0.23}(SO_4)_2(OH)_6$		
Space group			*R*-3*m*		
Unit cell dimensions (Å)					
a	7.2913(5)	7.2931(3)	7.2918(3)	7.2918(3)	7.2907(3)
c	17.1744(17)	17.1456(10)	17.1235(9)	17.1026(10)	17.0900(8)
V (Å^3)	790.72(11)	789.78(7)	788.48(6)	787.52(6)	786.70(6)
Z	3	3	3	3	3
Absorption coefficient	4.957 mm^{-1}	4.957 mm^{-2}	4.965 mm^{-3}	4.971 mm^{-3}	4.977 mm^{-3}
F(000)	742	742	742	742	742
q range	3.44 to 29.29°	3.44 to 29.29°	3.44 to 29.20°	3.44 to 29.21°	3.44 to 29.21°
Index ranges					
h	$-5 \le h \le 9$	$-9 \le h \le 7$	$-9 \le h \le 7$	$-9 \le h \le 7$	$-9 \le h \le 7$
k	$-9 \le k \le 7$	$-6 \le k \le 9$	$-6 \le k \le 9$	$-9 \le k \le 9$	$-9 \le k \le 9$
l	$-21 \le l \le 21$	$-21 \le l \le 21$	$-21 \le l \le 21$	$-21 \le l \le 21$	$-21 \le l \le 21$
Reflections collected/unique	1737 / 281	1741 / 278	1737 / 278	1733 / 277	1724 / 277
Reflections with $F > 4\sigma(F)$	260	257	259	257	256
Refinement method			Full-matrix least-squares on F^2		
Parameters refined	29	29	29	29	29
GoF	1.076	1.118	1.124	1.139	1.138
Final *R* indices [$F_o > 4\sigma(F)$]	$R_1 = 0.0215$, w$R_2 = 0.0246$	$R_1 = 0.0179$, w$R_2 = 0.0219$	$R_1 = 0.0196$, w$R_2 = 0.0235$	$R_1 = 0.0191$, w$R_2 = 0.0220$	$R_1 = 0.0179$, w$R_2 = 0.0213$
R indices (all data)	$R_1 = 0.0434$, w$R_2 = 0.0442$	$R_1 = 0.0367$, w$R_2 = 0.0376$	$R_1 = 0.0403$, w$R_2 = 0.0418$	$R_1 = 0.0398$, w$R_2 = 0.0406$	$R_1 = 0.0400$, w$R_2 = 0.0414$
Extinction coefficient	0.0000(3)	0.0002(3)	0.0005(3)	0.0004(3)	0.0005(3)
Largest diff. peak / hole	0.726 / –0.580 *e* Å^{-3}	0.343 / –0.673 *e* Å^{-3}	0.464 / –0.668 *e* Å^{-3}	0.406 / –0.868 *e* Å^{-3}	0.429 / –0.629 *e* Å^{-3}

Table 2: Fractional coordinates and atomic displacement parameters for jarosite.

297 K	*x*	*y*	*z*	U_{eq}	U_{11}	U_{22}	U_{33}	U_{23}	U_{13}	U_{12}
K	0	0	0	0.0160(4)	0.0185(5)	0.0185(5)	0.0112(8)	0	0	0.0092(3)
Fe	0.5	0	0.5	0.0056(2)	0.0036(3)	0.0018(3)	0.0108(3)	-0.0002(2)	-0.00010(11)	0.00088(15)
S	0	0	0.30862(7)	0.0074(3)	0.0059(4)	0.0059(4)	0.0102(6)	0	0	0.00297(18)
O1	0	0	0.6065(2)	0.0127(8)	0.0143(11)	0.0143(11)	0.0095(18)	0	0	0.0072(6)
O2	0.22287(15)	-0.22287(15)	-0.05403(12)	0.0114(5)	0.0131(8)	0.0131(8)	0.0122(10)	0.0006(4)	-0.0006(4)	0.0096(9)
O3	0.12713(16)	-0.12713(16)	0.13553(12)	0.0102(4)	0.0062(7)	0.0062(7)	0.0176(11)	-0.0021(4)	0.0021(4)	0.0026(8)
H1	0.188(2)	-0.188(2)	0.112(2)	0.044(13)						
253 K										
K	0	0	0	0.0137(3)	0.0151(4)	0.0151(4)	0.0108(7)	0	0	0.0076(2)
Fe	0.5	0	0.5	0.00447(19)	0.0026(2)	0.0013(3)	0.0091(3)	0.00007(19)	0.00003(9)	0.00065(13)
S	0	0	0.30880(6)	0.0066(2)	0.0054(3)	0.0054(3)	0.0091(5)	0	0	0.00270(16)
O1	0	0	0.60621(18)	0.0102(6)	0.0107(9)	0.0107(9)	0.0090(15)	0	0	0.0054(5)
O2	0.22272(13)	-0.22272(13)	-0.05393(10)	0.0106(4)	0.0115(7)	0.0115(7)	0.0127(10)	0.0007(3)	-0.0007(3)	0.0087(7)
O3	0.12679(14)	-0.12679(14)	0.13548(11)	0.0090(4)	0.0056(6)	0.0056(6)	0.0149(9)	-0.0013(3)	0.0013(3)	0.0021(7)
H1	0.186(2)	-0.186(2)	0.113(2)	0.030(10)						
213 K										
K	0	0	0	0.0117(3)	0.0127(5)	0.0127(5)	0.0098(7)	0	0	0.0063(2)
Fe	0.5	0	0.5	0.0038(2)	0.0020(2)	0.0009(3)	0.0081(3)	-0.0001(2)	-0.00005(10)	0.00044(15)
S	0	0	0.30890(7)	0.0057(3)	0.0044(4)	0.0044(4)	0.0085(6)	0	0	0.00219(18)
O1	0	0	0.6059(2)	0.0100(7)	0.0105(10)	0.0105(10)	0.0090(17)	0	0	0.0053(5)
O2	0.22258(15)	-0.22258(15)	-0.05377(11)	0.0088(4)	0.0098(7)	0.0098(7)	0.0101(10)	-0.0001(4)	0.0001(4)	0.0072(8)
O3	0.12696(16)	-0.12696(16)	0.13539(12)	0.0082(4)	0.0053(6)	0.0053(6)	0.0135(10)	-0.0011(4)	0.0011(4)	0.0022(8)
H1	0.188(2)	-0.188(2)	0.113(2)	0.032(11)						
173 K										
K	0	0	0	0.0097(3)	0.0106(4)	0.0106(4)	0.0079(7)	0	0	0.0053(2)
Fe	0.5	0	0.5	0.0031(2)	0.0014(2)	0.0004(3)	0.0072(3)	-0.00001(19)	-0.00001(10)	0.00021(14)
S	0	0	0.30903(6)	0.0052(3)	0.0040(3)	0.0040(3)	0.0076(5)	0	0	0.00200(17)

O1	0	0	0.60547(19)	0.0089(7)	0.0085(10)	0.0085(10)	0.0098(17)	0	0	0.0043(5)
O2	0.22269(14)	-0.22269(14)	-0.05367(11)	0.0080(4)	0.0083(7)	0.0083(7)	0.0105(10)	0.0002(3)	-0.0002(3)	0.0065(7)
O3	0.12696(15)	-0.12696(15)	0.13533(11)	0.0073(4)	0.0041(6)	0.0041(6)	0.0133(10)	-0.0012(4)	0.0012(4)	0.0017(7)
H1	0.189(2)	-0.189(2)	0.113(2)	0.036(12)						
133 K										
K	0	0	0	0.0076(3)	0.0080(4)	0.0080(4)	0.0066(6)	0	0	0.0040(2)
Fe	0.5	0	0.5	0.00252(19)	0.0008(2)	0.0000(3)	0.0065(3)	-0.00011(18)	-0.00006(9)	0.00001(13)
S	0	0	0.30918(6)	0.0046(2)	0.0032(3)	0.0032(3)	0.0075(5)	0	0	0.00158(16)
O1	0	0	0.60530(19)	0.0078(6)	0.0070(9)	0.0070(9)	0.0093(16)	0	0	0.0035(5)
O2	0.22253(13)	-0.22253(13)	-0.05352(10)	0.0069(4)	0.0062(6)	0.0062(6)	0.0098(9)	0.0000(3)	0.0000(3)	0.0041(7)
O3	0.12697(14)	-0.12697(14)	0.13524(11)	0.0064(4)	0.0041(6)	0.0041(6)	0.0115(9)	-0.0012(3)	0.0012(3)	0.0024(7)
H1	0.188(2)	-0.188(2)	0.114(2)	0.018(9)						

449 Table 3: Selected bond lengths (Å), volume (Å^3) and distortion parameters in jarosite.
450

		297 K	253 K	213 K	173 K	133 K
K□O3	x6	2.828(2)	2.8215(18)	2.819(2)	2.8157(19)	2.8129(18)
K□O2	x6	2.964(2)	2.9615(17)	2.9581(18)	2.9585(17)	2.9552(17)
<K□O>		2.896	2.892	2.889	2.887	2.884
Vol.		60.544(71)	60.298(61)	60.133(68)	60.07(64)	59.895(61)
Distortion		0.0168(1)	0.0165(1)	0.0161(1)	0.0158(1)	0.0155(1)
Fe□O3	x4	1.9785(8)	1.9778(7)	1.9783(8)	1.9784(7)	1.9784(7)
Fe□O2	x2	2.060(2)	2.0585(17)	2.0580(19)	2.0579(18)	2.0582(17)
<Fe□O>		2.006	2.005	2.005	2.005	2.005
Vol.		10.747(17)	10.727(14)	10.730(15)	10.731(15)	10.732(14)
Distortion		0.0014(1)	0.0014(1)	0.0014(1)	0.0014(1)	0.0015(1)
S□O1		1.457(4)	1.457(3)	1.460(4)	1.462(4)	1.462(3)
S□O2	x3	1.483(2)	1.4854(17)	1.4862(19)	1.4849(18)	1.4865(17)
<S□O>		1.477	1.478	1.480	1.479	1.480
Vol.		1.653(5)	1.658(4)	1.662(5)	1.661(5)	1.665(4)
O3□H1		0.87(3)	0.85(2)	0.87(3)	0.86(3)	0.86(2)

451
452
453 Table 4: Single crystal unit-cell parameters (Å) of jarosite.
454

	297 K	253 K	213 K	173 K	133 K
a	7.2913(5)	7.2931(3)	7.2918(3)	7.2918(3)	7.2907(3)
c	17.1744(17)	17.1456(10)	17.1235(9)	17.1026(10)	17.0900(8)
V	790.72(11)	789.78(7)	788.48(6)	787.52(6)	786.70(6)

Figure 1a.

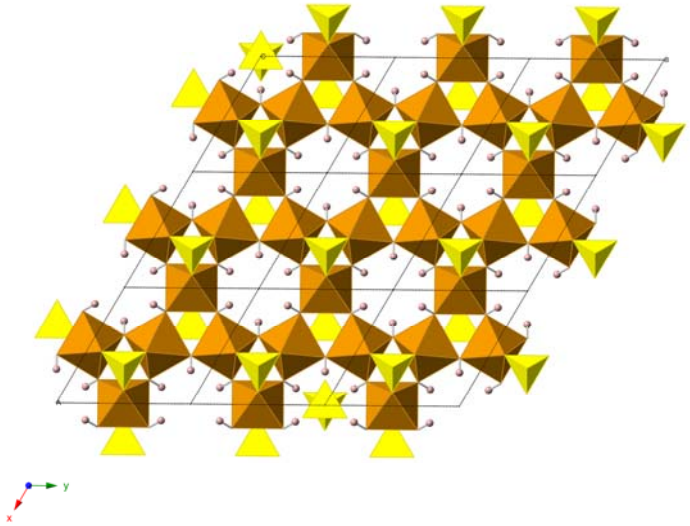

Figure 1b.

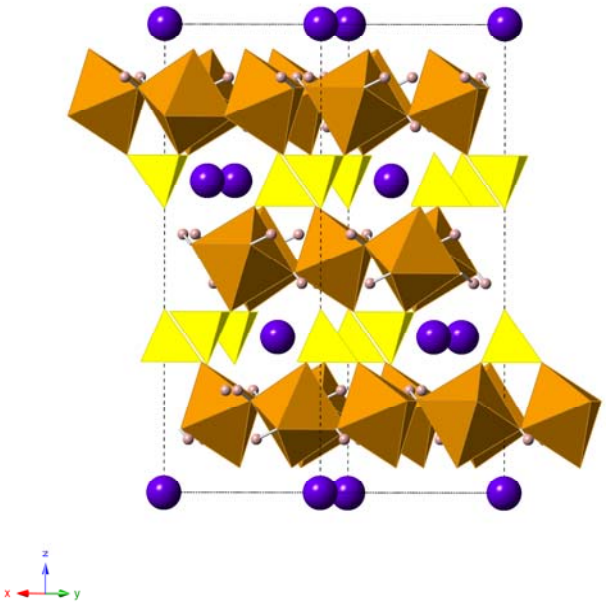

Figure 2a.

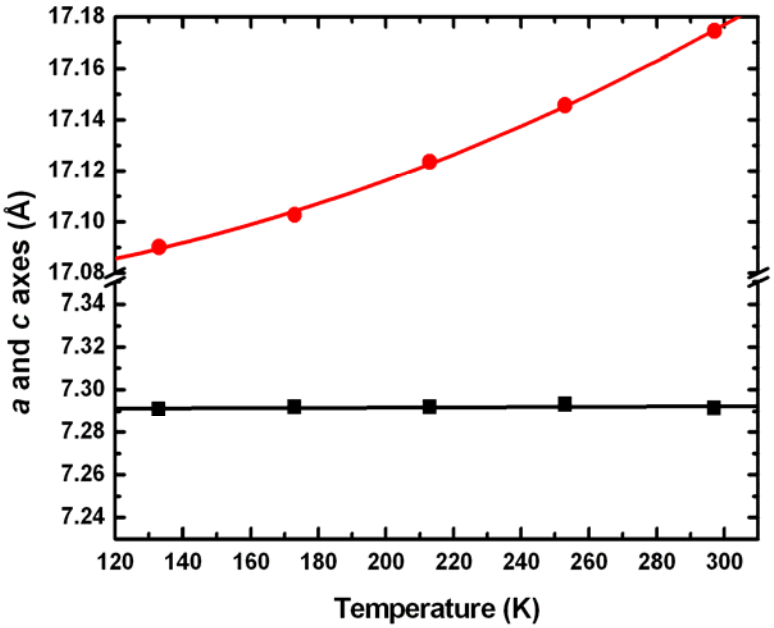

Figure 2b.

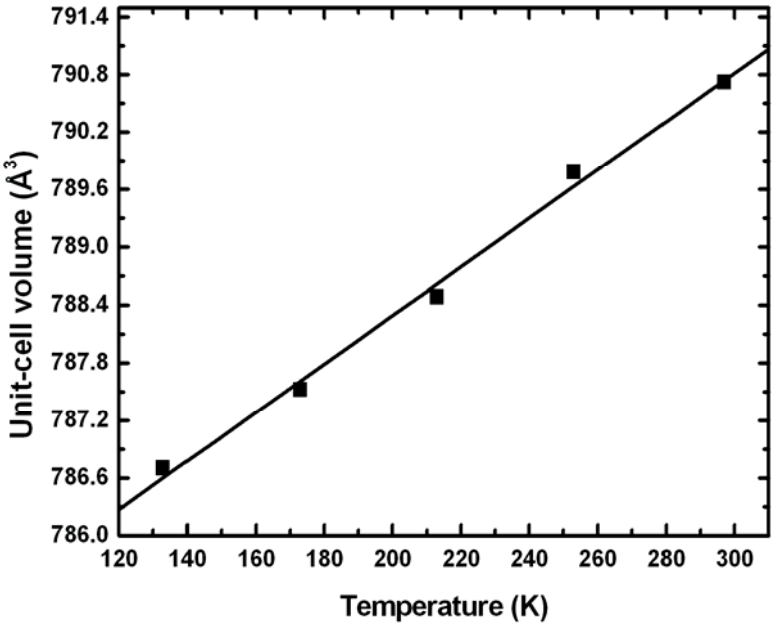

476 Figure 3a.
477

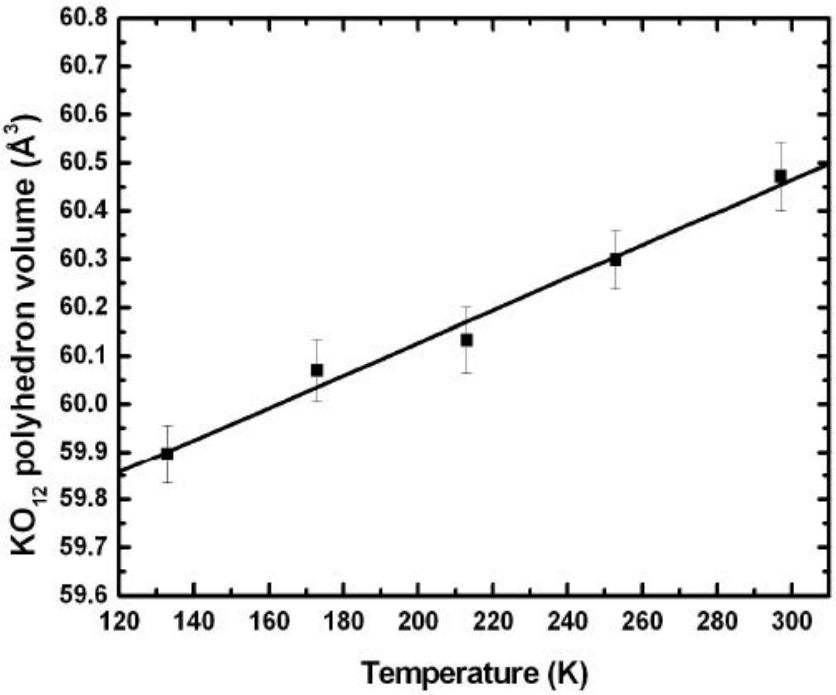

478
479 Figure 3b.

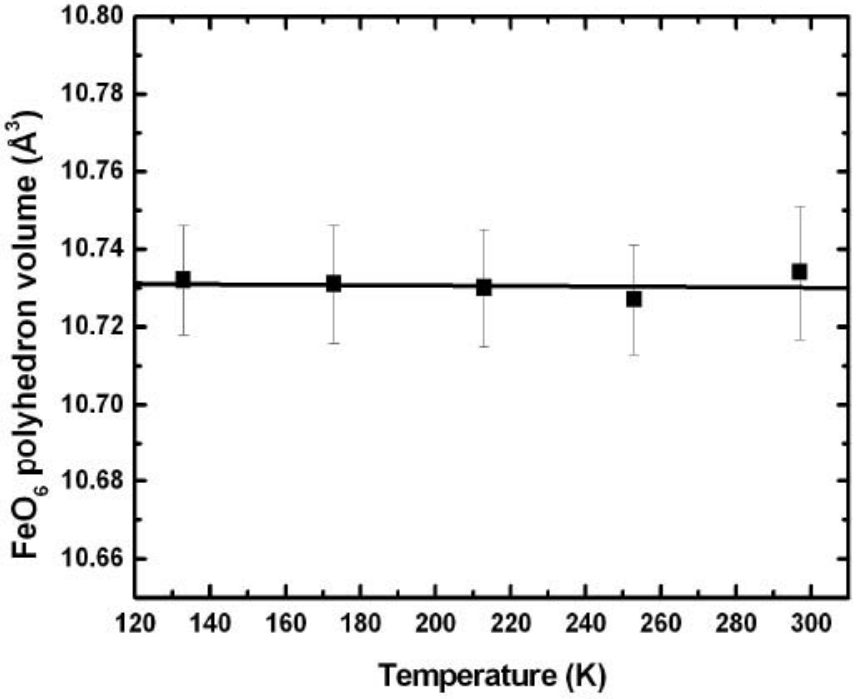

480

Figure 3c.

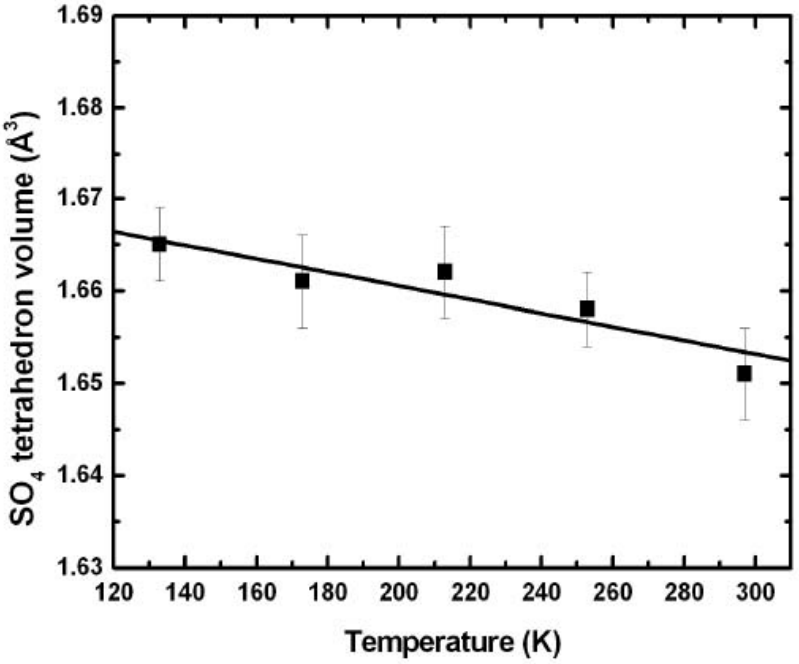

Figure 4a.

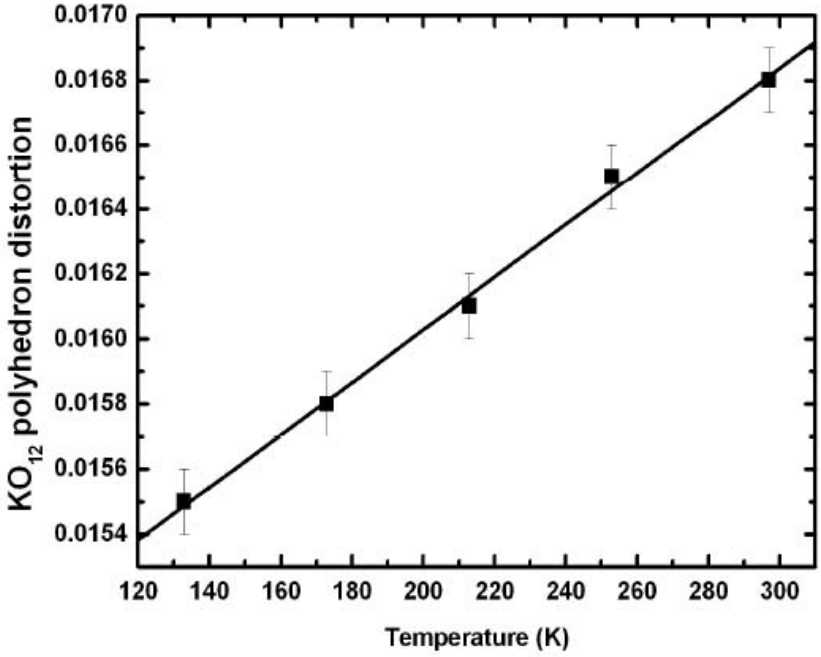

Figure 4b.

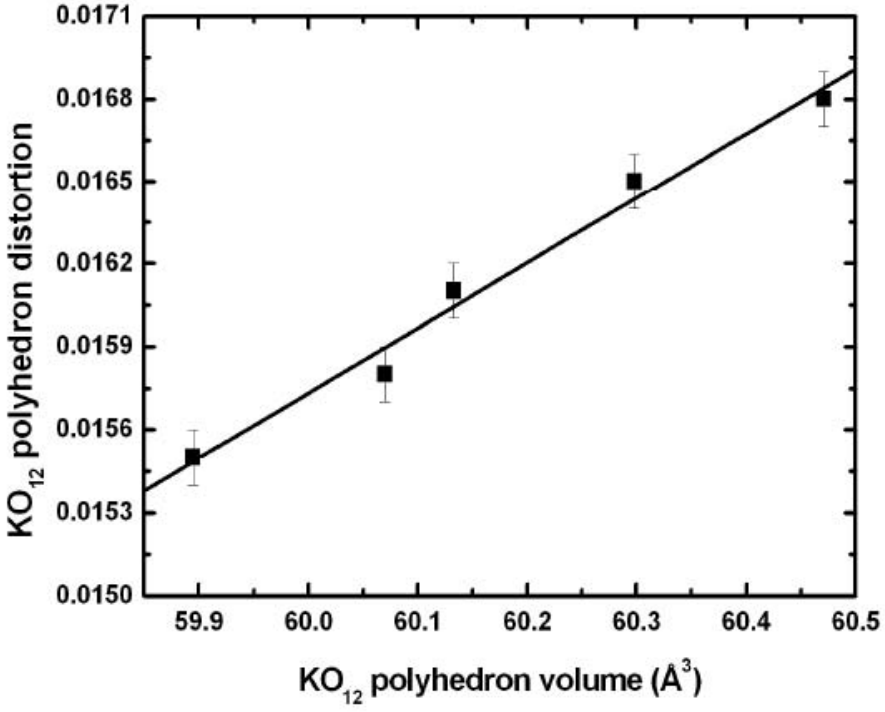

Figure 4c.

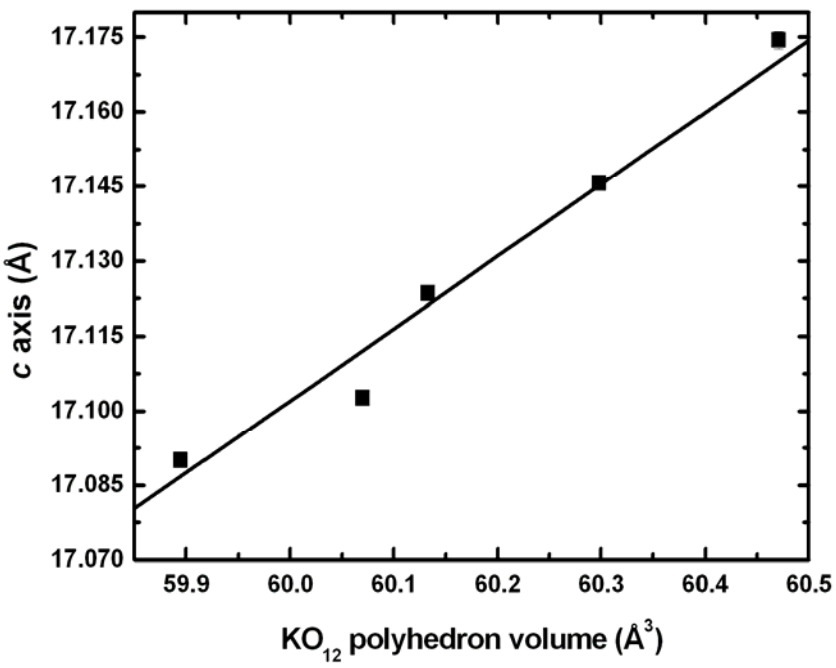

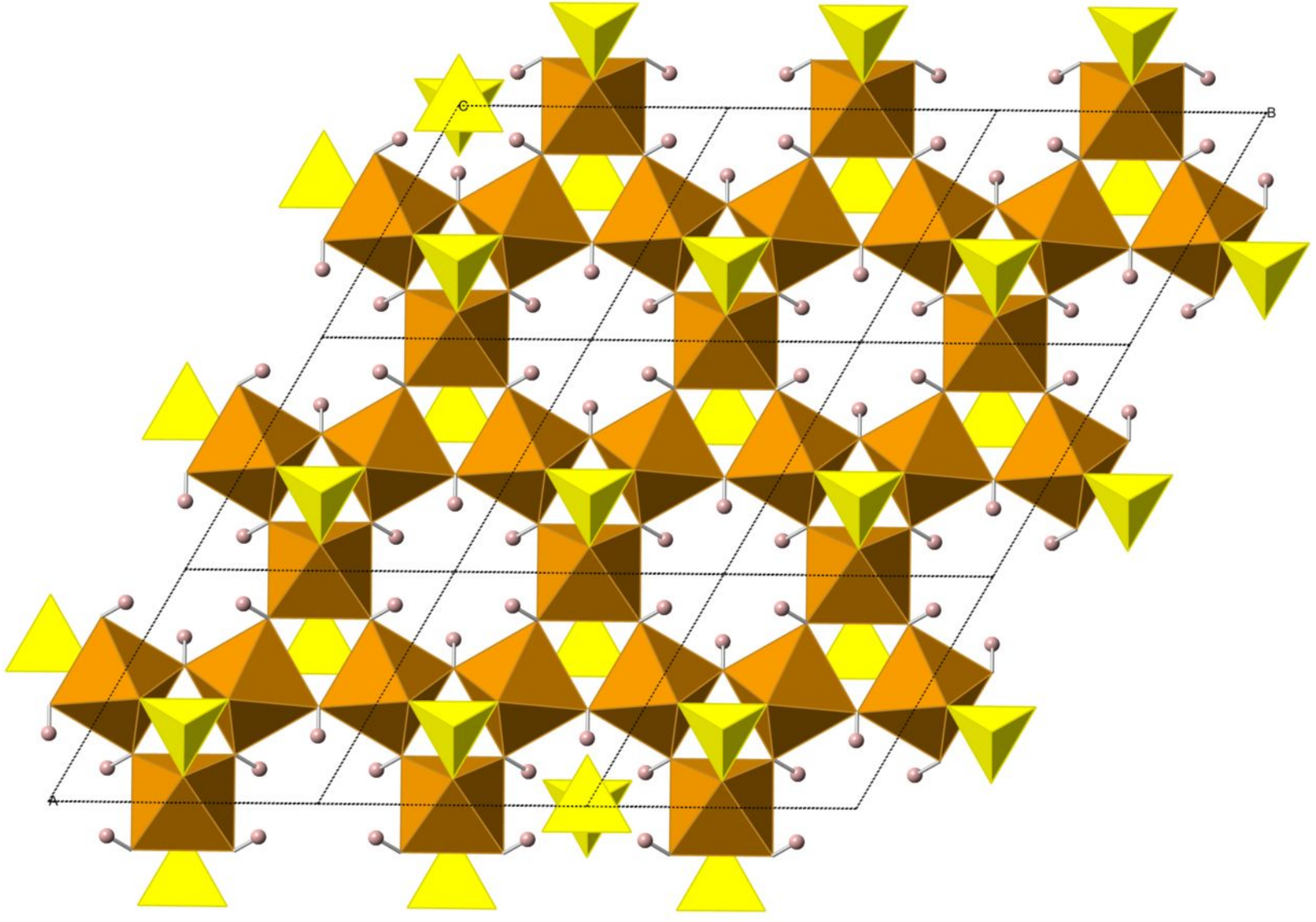
C
B
A

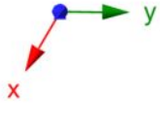
y
x

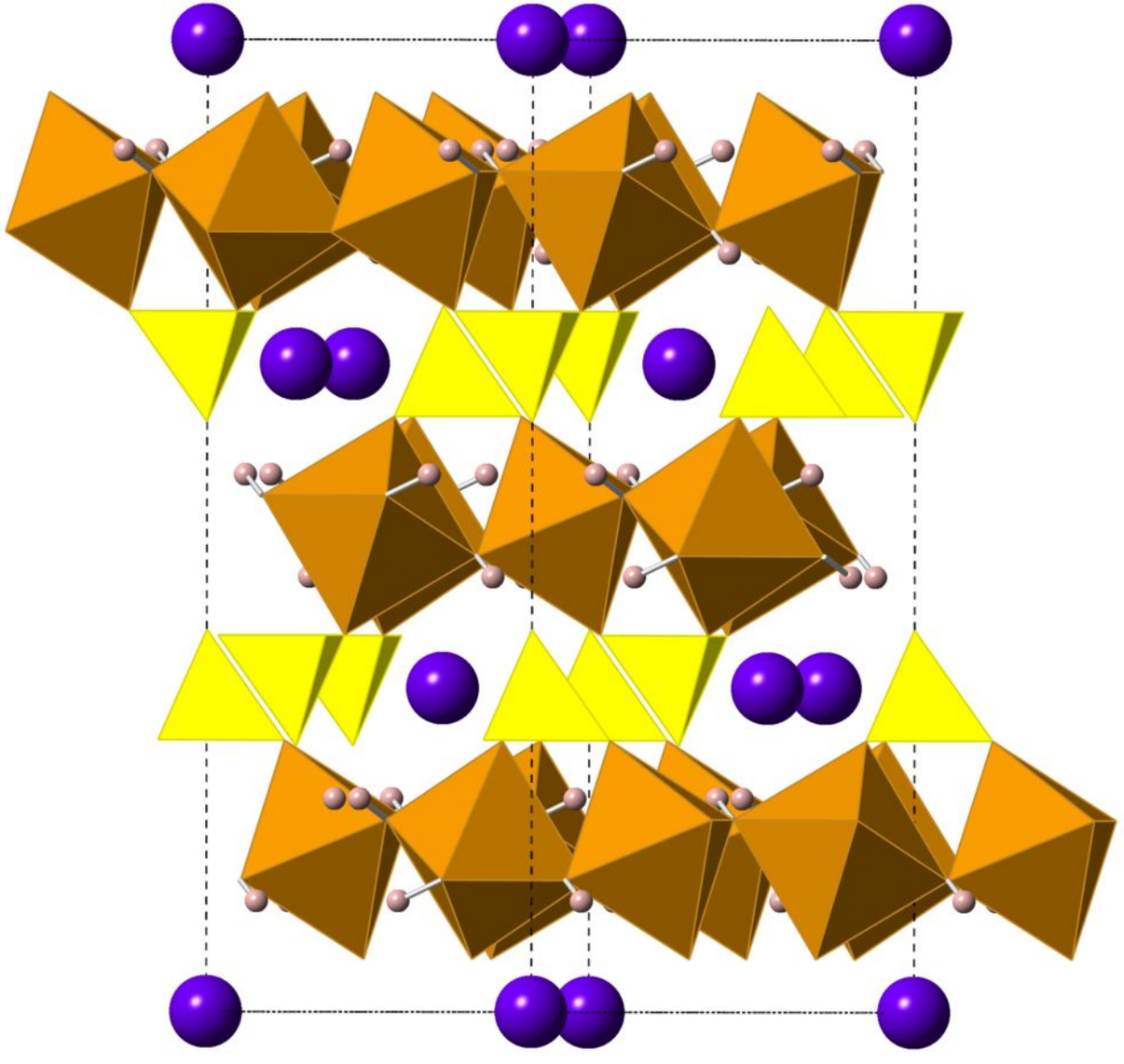
z
x
y

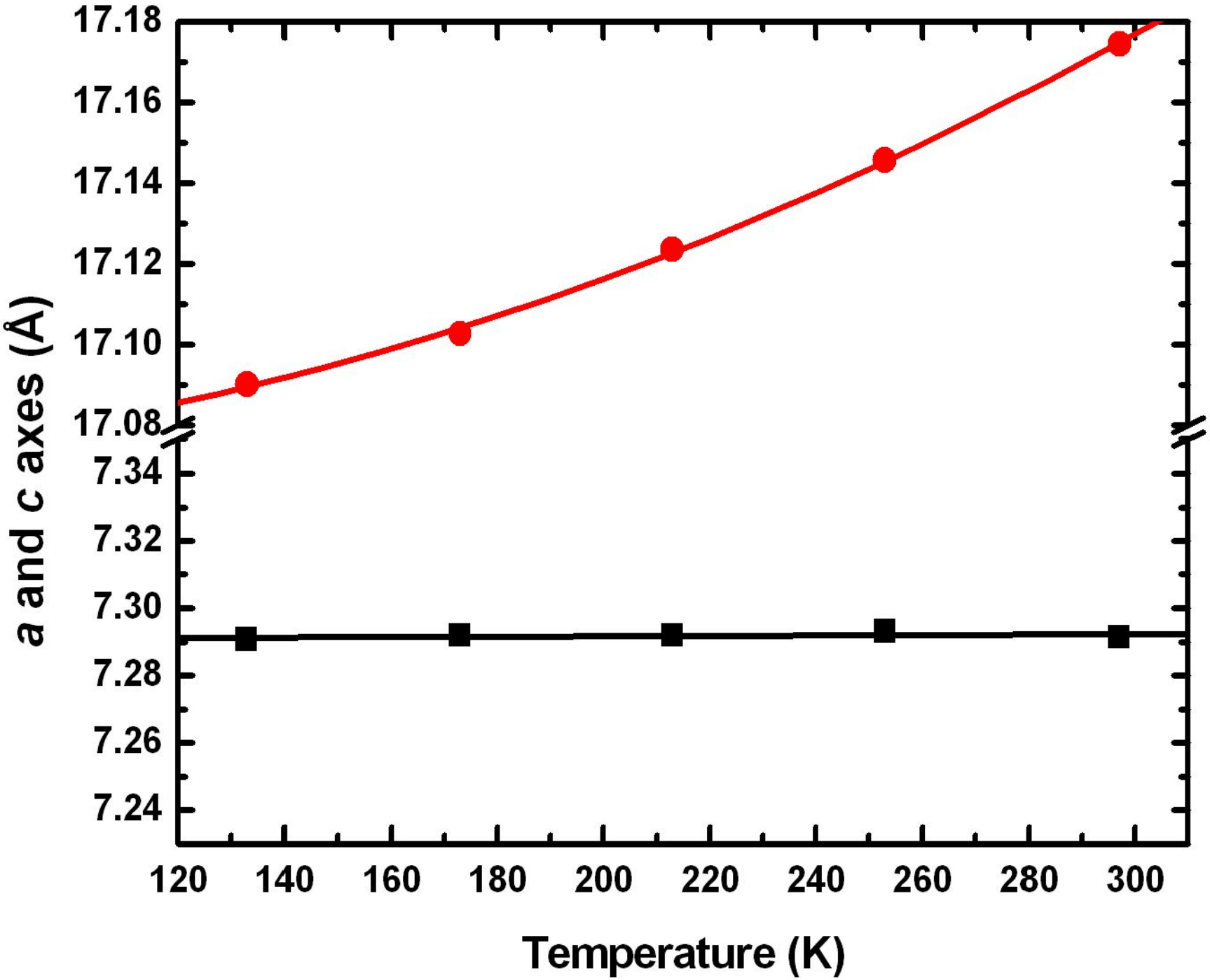

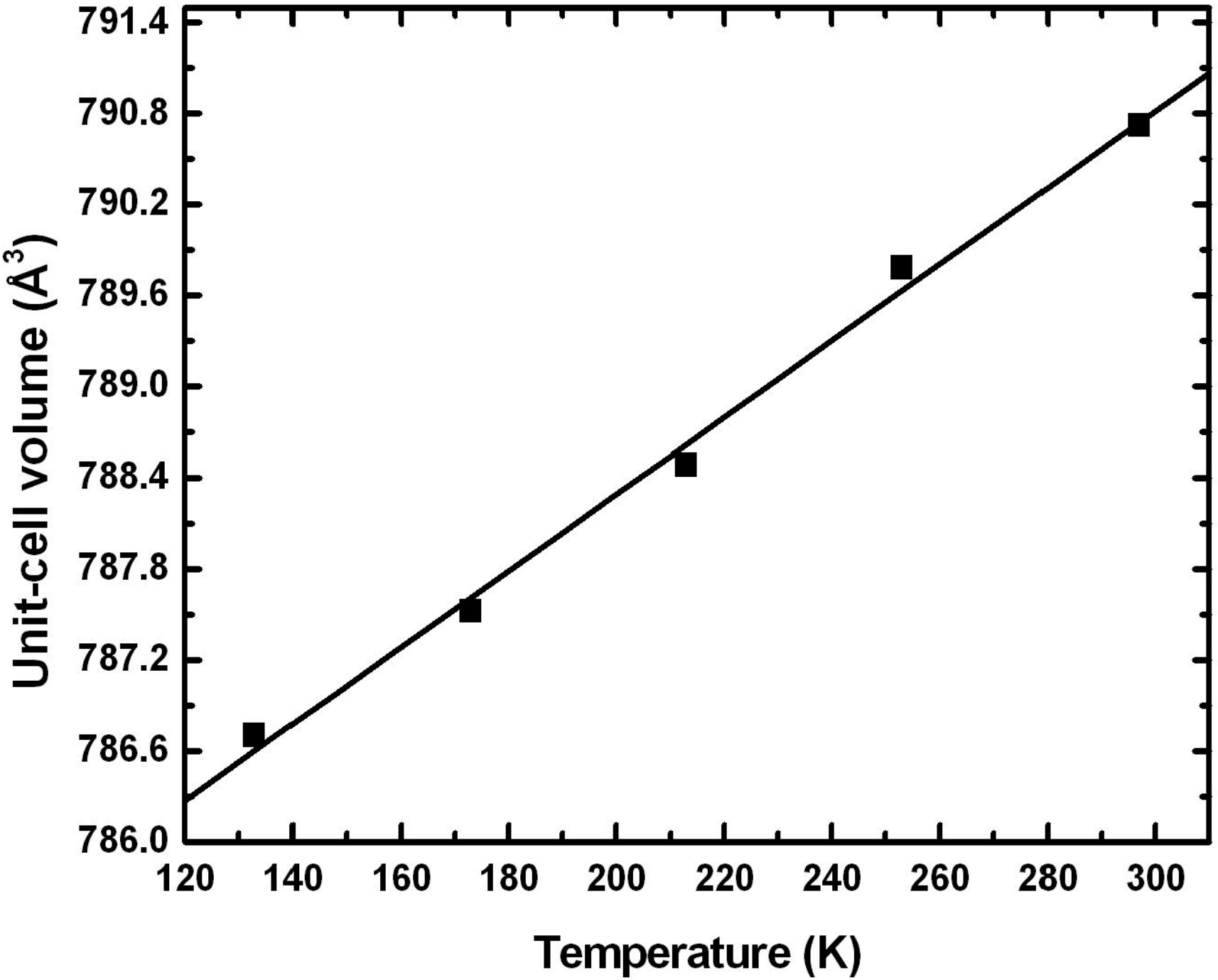
Unit-cell volume (Å^3)
791.4
790.8
790.2
789.6
789.0
788.4
787.8
787.2
786.6
786.0
120
140
160
180
200
220
240
260
280
300
Temperature (K)

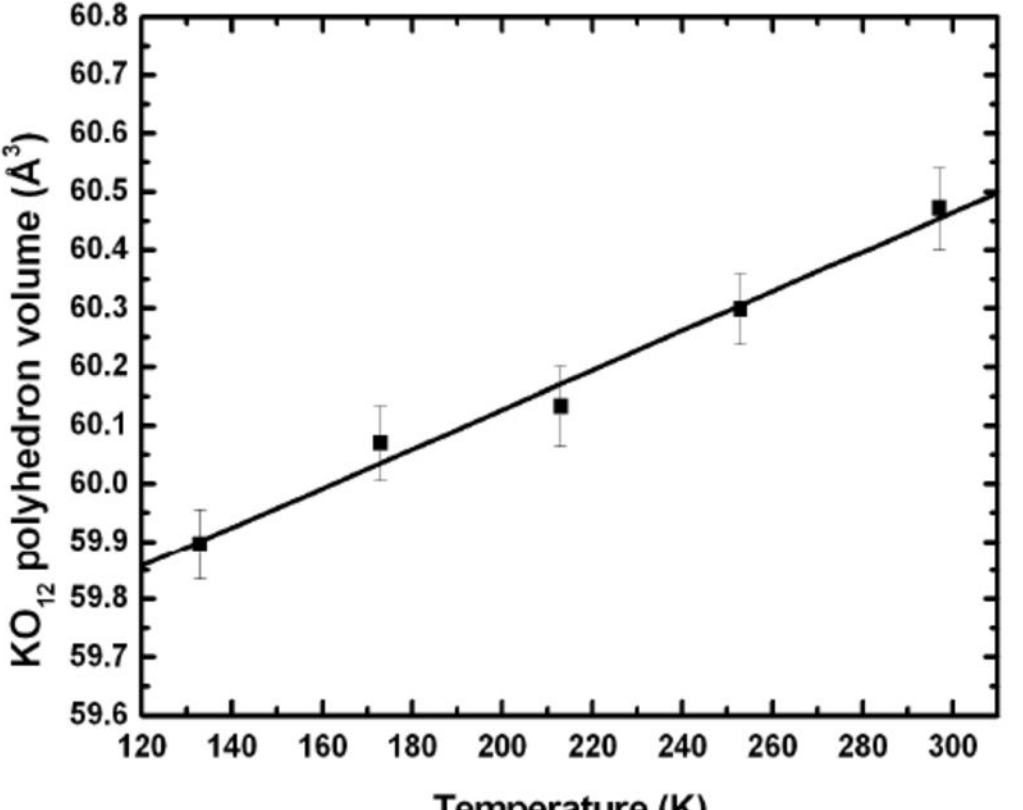

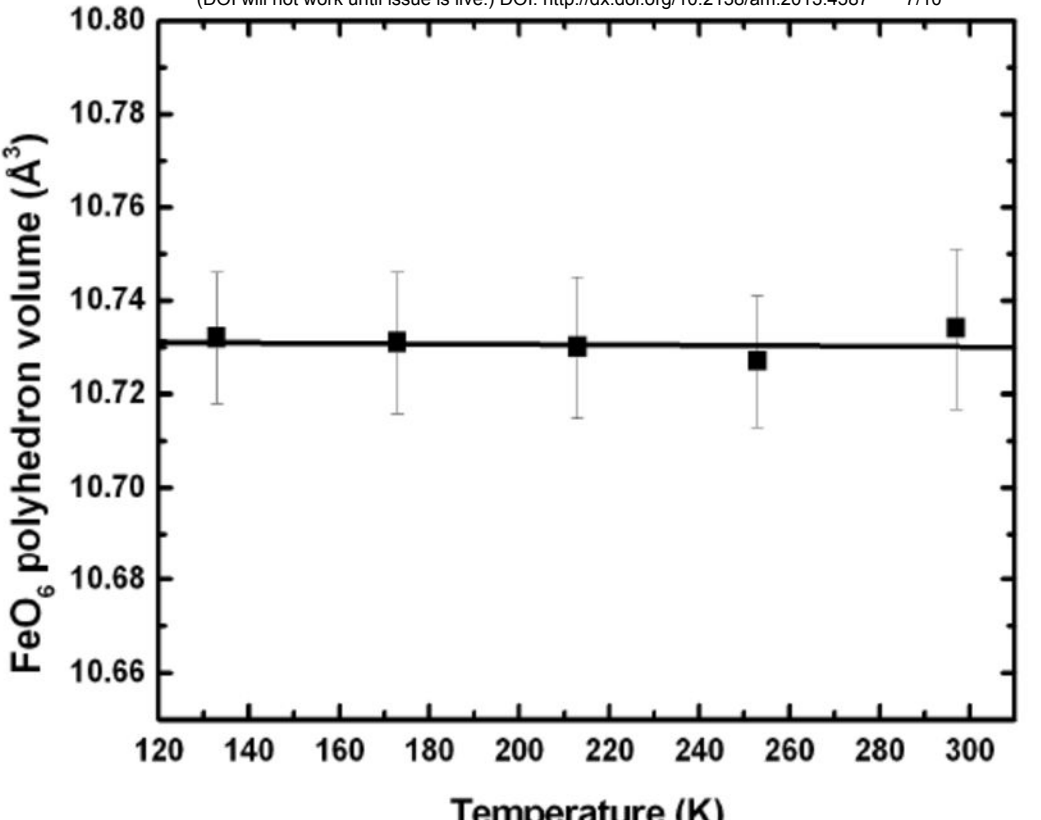
10.80
10.78
10.76
10.74
10.72
10.70
10.68
10.66
FeO6 polyhedron volume (Å3)
120
140
160
180
200
220
240
260
280
300
Temperature (K)

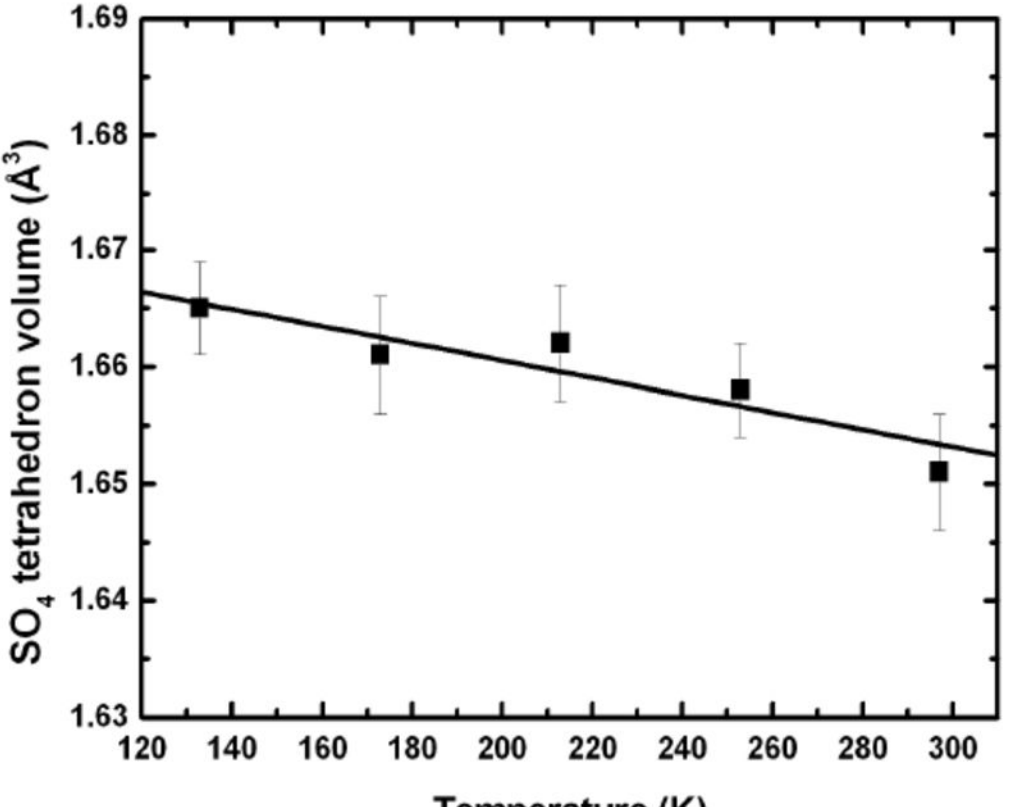

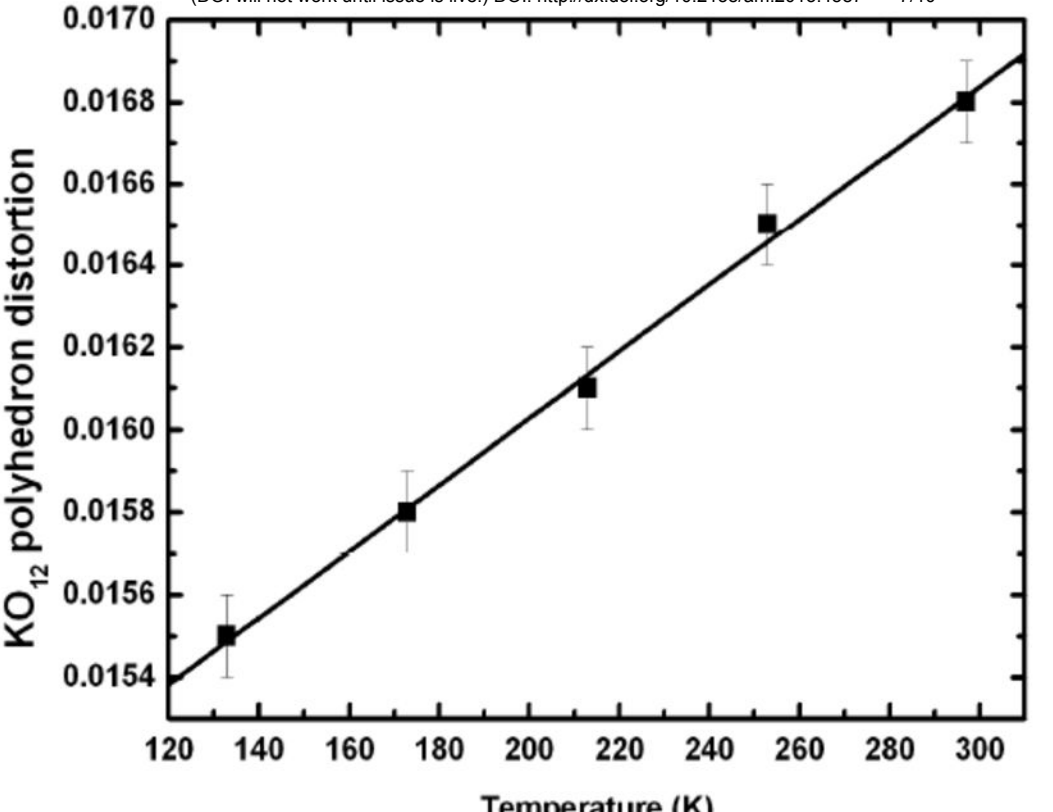
0.0170
0.0168
0.0166
0.0164
0.0162
0.0160
0.0158
0.0156
0.0154
KO_{12} polyhedron distortion
120
140
160
180
200
220
240
260
280
300
Temperature (K)

This is a preprint, the final version is subject to change, of the American Mineralogist (MSA)
Cite as Authors (Year) Title. American Mineralogist, in press.
(DOI will not work until issue is live.) DOI: http://dx.doi.org/10.2138/am.2013.4587